

Intensity-based Segmentation of Tissue Images Using a U-Net with a Pretrained ResNet-34 Encoder: Application to Mueller Microscopy

Sooyoung Chae^{1*†}, Dani Giammattei^{2*}, Ajmal Ajmal², Junzhu Pei², Amanda Sanchez²,
 Tananant Boonya-ananta², Andres Rodriguez², Tatiana Novikova^{1,2}, and Jessica
 Ramella-Roman^{2,3}

¹LPICM, CNRS, École Polytechnique, IP Paris, 91120 Palaiseau, France

²Department of Biomedical Engineering, Florida International University, Miami, FL
 33174, USA

³Department of Ophthalmology, Herbert Wertheim College of Medicine, Florida
 International University, Miami, FL 33199, USA

*These authors contributed equally to this work.

†sooyong.chae@polytechnique.edu

Abstract

Manual annotation of the images of thin tissue sections remains time-consuming step in Mueller microscopy and limits its scalability. We present a novel automated approach using only the total intensity M_{11} element of the Mueller matrix as an input to a U-Net architecture with a pretrained ResNet-34 encoder. The network was trained to distinguish four classes in the images of murine uterine cervix sections: background, internal os, cervical tissue, and vaginal wall. With only 70 cervical tissue sections, the model achieved 89.71% pixel accuracy and 80.96% mean tissue Dice coefficient on the held-out test dataset. Transfer learning from ImageNet enables accurate segmentation despite limited size of training dataset typical of specialized biomedical imaging. This intensity-based framework requires minimal preprocessing and is readily extensible to other imaging modalities and tissue types, with publicly available graphical annotation tools for practical deployment.

1 Introduction

Imaging Mueller polarimetry has been extensively explored for biomedical applications [1, 2, 3, 4]. For quantitative analysis in Mueller matrix (MM) microscopy, accurate anatomical segmentation is a necessary for obtaining structure-specific polarimetric maps. Physical realizability (PR) test of the MM [5, 6] remains the first step of experimental polarimetric data post-processing. As demonstrated in our previous work [7], the PR test serves as an effective physics-informed filter for the MM images of bulk tissues, naturally retaining tissue regions, while excluding background and non-physical artifacts.

However, thin tissue sections exhibit weak polarimetric response with diagonal MM elements close to unity and reduced image contrast, making PR-based filtering less effective. Despite this reduced contrast, polarimetric information remains detectable in the polarimetric images of thin sections: linear retardance LR and optical axis orientation ψ exhibit spatial patterns corresponding to anisotropic tissue organization (Fig. 1). For example, several studies have demonstrated that polarimetric imaging characterizes cervical collagen organization [8, 9] and detects its remodeling during pregnancy [10, 11].

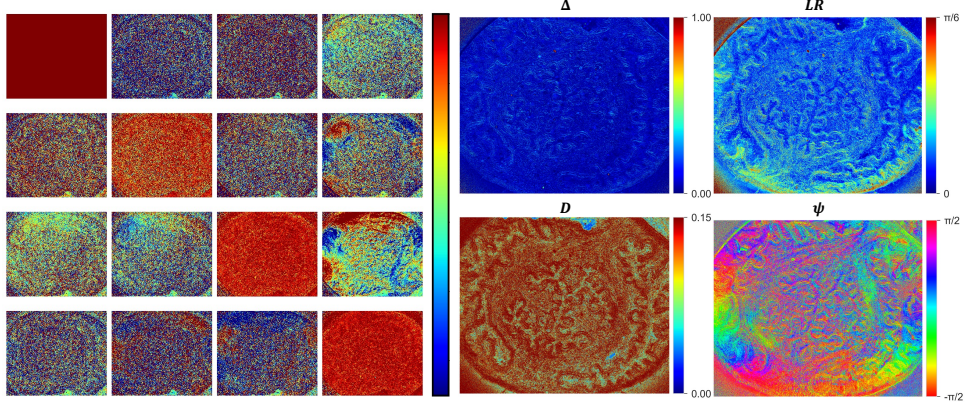


Figure 1: Images of murine uterine cervix thin section (Day 18 of the gestation). **Left:** MM images. Color bar: $[0, 1]$ (diagonal elements), $[-0.1, 0.1]$ (off-diagonal elements). **Right:** Derived maps of polarimetric parameters using Lu-Chipman decomposition [12]: depolarization Δ (dimensionless), diattenuation D (dimensionless), linear retardance LR (rad), and optical axis azimuth ψ (rad).

To enable structure-specific polarimetric analysis, accurate segmentation of anatomical regions is required [13, 14]. While the M_{11} element provides sufficient morphological contrast for this task, manual annotation of tissue regions and anatomical structures remains tedious and time-consuming, limiting scalability. Deep learning offers automated segmentation, but typically requires hundreds to thousands of annotated samples [15] — a limitation when sample acquisition involves animal protocols, histological preparation, and custom instrumentation. We demonstrate that, when imaging cervical samples, the transfer learning from ImageNet-pretrained networks enables accurate tissue segmentation from MM data using only 70 annotated sample images.

We employ a U-Net architecture [15] with pretrained ResNet-34 encoder [16] for pixel-wise segmentation using only the image of M_{11} element of MM. This intensity-based approach requires minimal preprocessing compared to full MM decomposition and leverages natural image features learned from ImageNet to identify structural patterns in sample images. We provide an intuitive graphical interface for annotation and model deployment, enabling practical implementation without extensive programming.

2 Instrumentation

MM images of thin cervical tissue sections were acquired using a custom transmission-mode MM polarimeter built on a commercial trinocular microscope (ME580T-PZ-2L, AmScope). Samples were illuminated with a 9W stabilized broadband source (SLS201L, Thorlabs) filtered at 550 nm (FB550-10-1, Thorlabs). Complete 4×4 MM images were reconstructed from 16 intensity images acquired under different polarization states generated by a motorized Polarization State Generator (PSG) and analyzed by a Polarization State Analyzer (PSA). Each comprised a linear polarizer (LPVISC100, Thorlabs) and motorized quarter-wave plate (AQWP10M-580, Thorlabs) on a rotation stage (PRM1Z8, Thorlabs). Samples were imaged with a $5 \times$ objective (NA 0.13, 4 mm field of view) and recorded with a 16-bit sCMOS camera (PCO.edge 5.5) with an image size of 2560×2160 pixels and resolution of $\sim 1.5 \mu\text{m}$ per pixel.

3 Sample Collection and Annotation

Cervical tissue was selected as a representative anatomical challenge due to its heterogeneous structure and the morphological changes it undergoes across gestation. The dataset comprised 70 thin ($\sim 50 \mu\text{m}$) sections of murine uterine cervix across early to late gestation periods (Days 0 – 18). To generate ground truth segmentation masks from this small dataset, we developed a custom annotation tool using PyQt5 [17]. The software displays pixel-wise normalized M_{11} intensity images and provides interactive polygon and freehand drawing modes for delineating the regions of interest (Fig. 2).

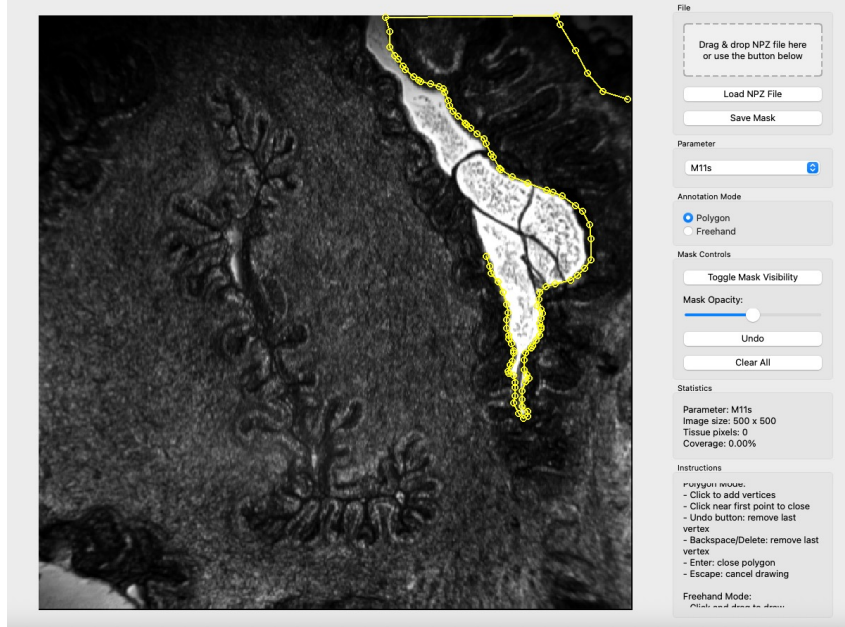


Figure 2: Screenshot of the custom Tissue Annotation Tool GUI. The interface features an interactive canvas for visualizing the normalized M_{11} intensity map. The control panel enables users to switch between vertex-based Polygon and Freehand drawing modes, adjust mask layer opacity, and define the semantic classes (e.g., internal os, vaginal wall)

Separate binary masks were created for general tissue, internal os, and vaginal wall, then combined into four-class maps with priority hierarchy: vaginal wall (class 3) > OS (class 2) > tissue (class 1) > background (class 0). The tool is distributed as standalone executables for macOS and Windows to ensure accessibility without programming expertise (see Code Availability). Manual annotation shows notable morphological variability across samples (Fig. 3).

Tissue boundaries exhibited ambiguity from preparation-related damage, internal os shapes varied substantially, and vaginal wall presence ranged from complete to absent depending on sectioning depth. This heterogeneity, combined with the small sample size, presents a challenging test case for deep learning generalization.

The dataset was stratified by acquisition day and split into training (49 samples, 70%), validation (10 samples, 15%), and test (11 samples, 15%) sets to ensure generalization and prevent data leakage between experimental sessions.

4 Methods

We employed a U-Net architecture [15] with a pretrained ResNet-34 encoder [16] for pixel-wise classification into four classes: background, general tissue, internal os, and vaginal wall. The

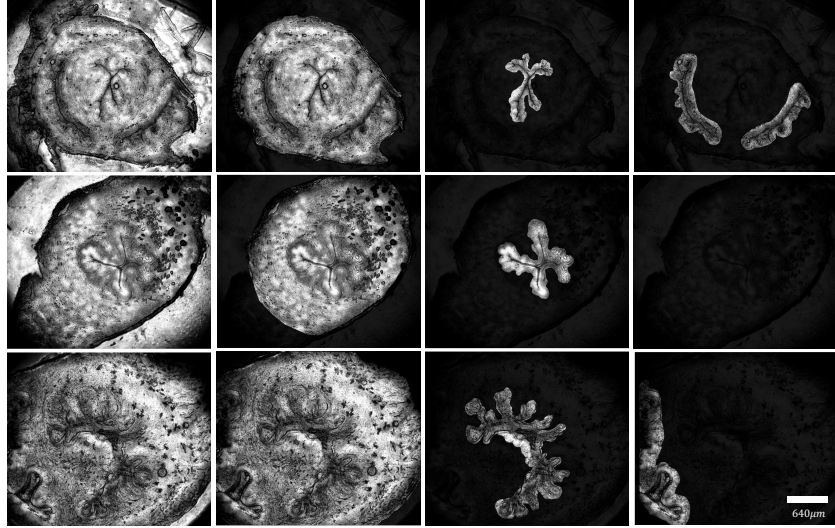


Figure 3: Representative images of cervical tissue sections. **Left to Right:** M_{11} intensity image, tissue mask, OS mask, and vaginal wall mask. **Top:** Clear OS and vaginal wall structures. **Middle:** Absent vaginal walls. **Bottom:** Irregular internal vaginal wall shapes and ambiguous tissue borders.

model architecture is shown in Fig 4. The encoder (initialized with ImageNet-1K v1 pretrained weights [18]) progressively downsamples the input (512×512 pixels) through five blocks with channel dimensions [64, 64, 128, 256, 512]. Input M_{11} images were resized to 512×512 pixels using bilinear interpolation, while corresponding masks were resized using nearest-neighbor interpolation to preserve discrete class labels [19].

Single-channel M_{11} images were replicated to three channels and normalized using ImageNet statistics (mean=[0.485, 0.456, 0.406], std=[0.229, 0.224, 0.225]) to ensure compatibility with pretrained weights. The decoder reconstructs spatial resolution via skip connections and bilinear upsampling, applying convolution-BatchNorm-ReLU blocks [20] to produce four-channel output logits.

Training used a combined loss ($\mathcal{L}_{\text{total}} = 0.5 \cdot \mathcal{L}_{\text{CE}} + 0.5 \cdot \mathcal{L}_{\text{Dice}}$) balancing cross-entropy and Dice loss [21], with AdamW optimizer [22] (learning rate 1×10^{-4} , weight decay 1×10^{-5}), batch size of 8, and 50 epochs. The best model was selected based on minimum validation loss. Data augmentation included random horizontal/vertical flips, 90-degree rotations, and intensity jittering ($\pm 15\%$). The dataset was stratified by acquisition day (70% training, 15% validation, 15% testing) for generalization. All experiments were conducted using PyTorch [23] with mixed-precision training [24] on NVIDIA GPU (RTX5000 ADA, 16Go DDR6).

5 Results

The model achieved 91.72% training accuracy and 89.66% validation accuracy after 50 epochs, with validation loss converging to 0.374 (Fig. 5). Close alignment between training and validation curves throughout training indicates effective generalization without overfitting.

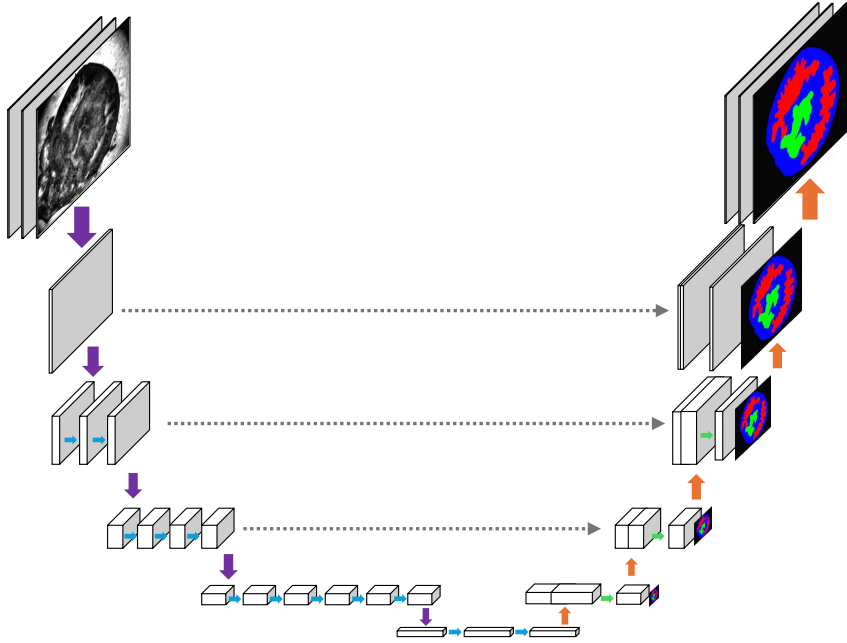


Figure 4: U-Net with a ResNet-34 encoder for M₁₁ tissue image segmentation. The encoder down-samples the input (purple arrows) with internal cross-layer connections (blue arrows). Skip connections (gray dashed arrows) pass high-resolution features to the decoder, which up-samples the features (orange arrows) with internal cross-layer connections (green arrows). Spatial resolution decreases from 256×256 to 16×16 at the bottleneck and increases to 512×512 at the output.

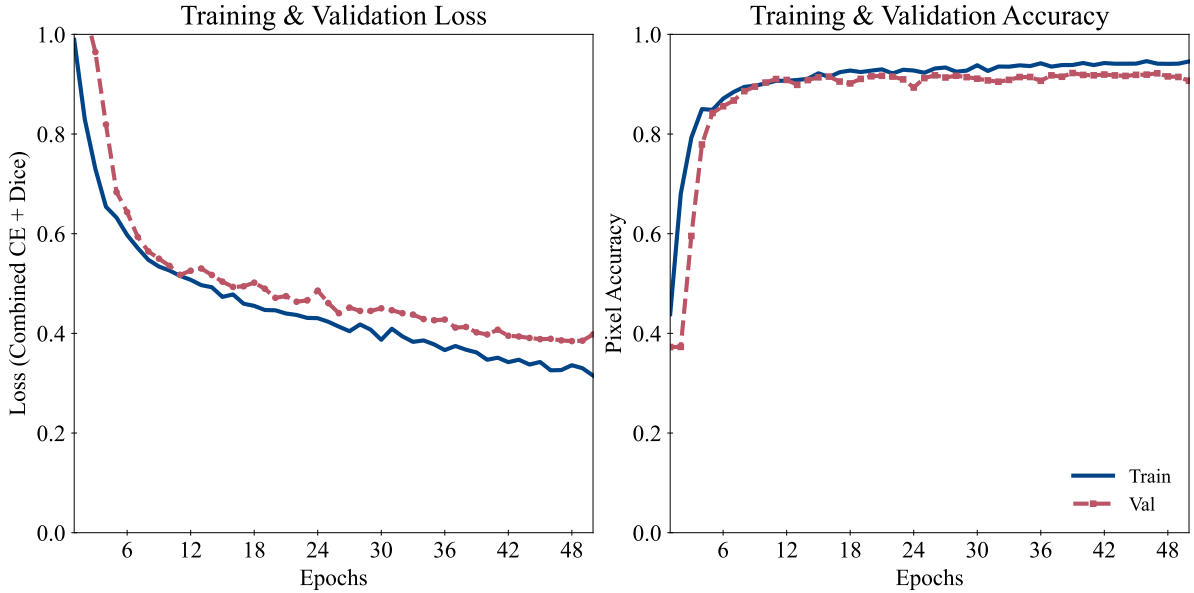


Figure 5: Training metrics over 50 epochs. **Left:** combined loss showing steady convergence. **Right:** pixel accuracy demonstrating robust generalization.

On the held-out test dataset (stratified by acquisition day), the model achieved $89.71\% \pm 5.51\%$ overall pixel accuracy and $80.96\% \pm 13.37\%$ mean tissue Dice coefficient (see Tab. 1).

Per-class performance showed accurate segmentation for background (DSC: $92.37\% \pm 9.42\%$), tissue ($88.63\% \pm 4.44\%$), and internal os ($84.85\% \pm 9.71\%$). The vaginal wall segmentation exhibited higher variance (DSC: $69.41\% \pm 32.61\%$) due to its anatomically variable presence

Table 1: Test dataset performance (mean \pm std, in %).

| Metric | Dice (%) | IoU (%) |
|-----------------|-----------------|-----------------|
| Pixel Accuracy | - | 89.7 ± 5.5 |
| Mean tissue DSC | 81.0 ± 13.4 | - |
| Background | 92.4 ± 9.4 | 87.1 ± 14.2 |
| Tissue | 88.6 ± 4.4 | 79.9 ± 7.1 |
| OS | 84.9 ± 9.7 | 74.8 ± 13.1 |
| Vaginal | 69.4 ± 32.6 | 60.7 ± 30.5 |

across sectioning depths and preparation artifacts, as seen in Figure 3. The overlap metric IoU (Intersection over Union) demonstrates similar trends. The representative model predictions are shown in Figure 6. The model accurately segments well-preserved samples (top), correctly predicts vaginal wall absence (middle), and can detect low-contrast structures missed during manual annotation (bottom), suggesting learned sensitivity to subtle polarimetric features.

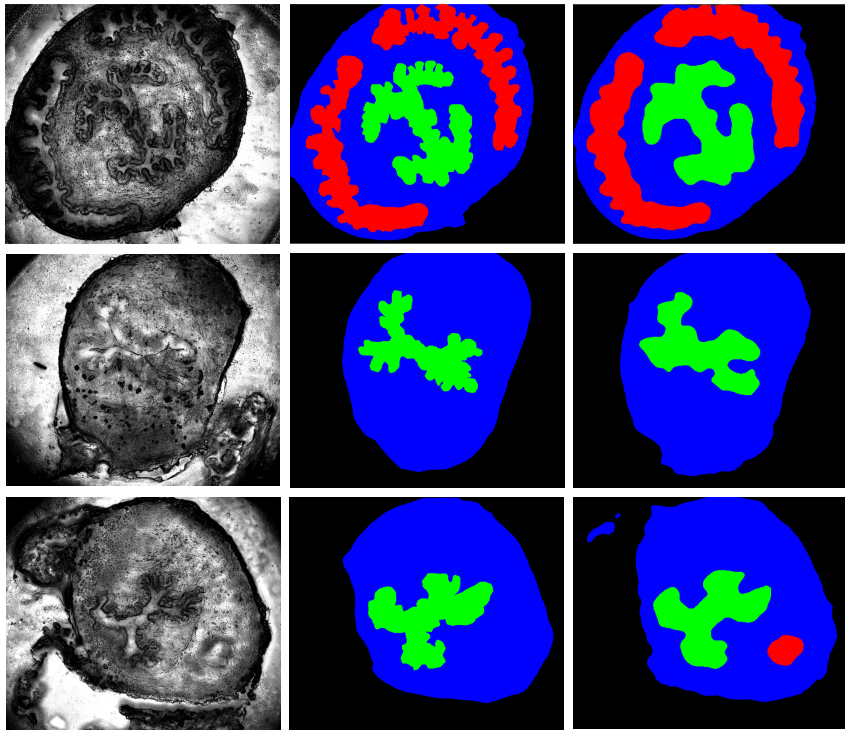


Figure 6: Successful segmentation cases. Columns - **Left**: total intensity (M_{11} images); **Middle**: ground truth images (blue=tissue, green=OS, red=vaginal wall); **Right**: model predictions (**top**) - clear boundaries; (**middle**) - correct absence of vaginal walls; (**bottom**) - detection of structure missed in manual annotation.

Fig. 7 illustrates the failure cases: the segmentation errors in damaged tissue (top) reflect ground truth ambiguity, while segmentation in poorly illuminated regions (bottom) shows degraded performance under low signal-to-noise conditions.

6 Discussion

We demonstrated automated tissue segmentation from Mueller microscopy measurements using only the intensity image (M_{11} element) as an input data. By leveraging transfer learning from

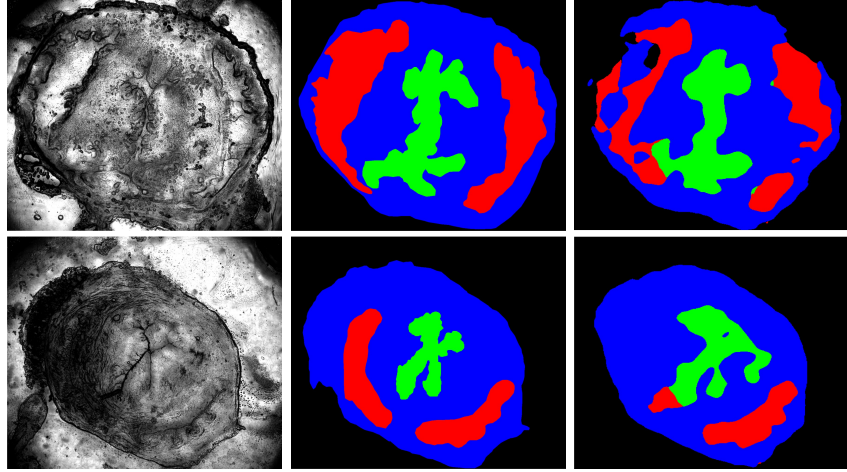


Figure 7: Failure cases. Columns - **Left**: total intensity (M_{11} images); **Middle**: ground truth images ; **Right**: model predictions **(top)** - segmentation errors because of tissue damage during preparation; **(bottom)** - under-performance of tissue segmentation because of poor illumination.

ImageNet-pretrained ResNet-34 weights, the approach achieved robust segmentation (89.71% pixel accuracy, 80.96% mean tissue DSC) with only 70 total samples (49 training, 11 validation, 10 test). This small dataset requirement addresses a critical bottleneck in biomedical applications of imaging polarimetry, where acquiring and annotating specialized tissue samples is labor-intensive and often limited by availability of specimens.

The success of our approach with limited training dataset demonstrates that pretrained encoders effectively transfer natural image features to polarimetric intensity patterns, requiring minimal domain-specific fine-tuning. This contrasts with training from scratch, which typically demands hundreds to thousands of annotated samples [15]. The single-channel intensity-based approach further reduces preprocessing complexity compared to full MM decomposition methods [7], enabling rapid deployment for biomedical workflows where annotation resources are scarce. Importantly, because our method relies only on the M_{11} total intensity images, it is extensible to other tissue types using other imaging modalities.

The model’s ability to detect low-contrast vaginal tissue missed during manual annotation (Fig. 6, bottom) suggests learned sensitivity to polarimetric intensity patterns beyond subjective human interpretation, reducing inter-observer variability. However, the high variance in vaginal wall segmentation ($69.41\% \pm 32.61\%$ DSC) reflects genuine biological variability—the structure’s presence depends on sectioning plane and depth, introducing fundamental uncertainty even in ground truth labels. The primary limitation of our small-sample approach is sensitivity to domain shift: samples with significantly different morphology may require additional training data for adaptation. Failure cases remain tied to sample preparation quality and imaging conditions (Fig. 7).

The framework’s accessibility—requiring only 50 annotated samples, normalized intensity images, and standard U-Net architecture enables straightforward extension to other tissue types and imaging modalities. Our graphical annotation tool and trained models are publicly available, providing a practical pipeline for the analysis of MM images of tissues in resource-limited settings where large-scale annotation is impractical.

Acknowledgments

SC, TN acknowledge support from the EUR BERTIP (ANR 18EURE0002, Program France 2030) and European Cooperation in Science and Technology (COST) actions CA21159 PhoBioS

and CA23125 TETRA. JRR acknowledges support from the National Science Foundation (NSF) Award #DMR-1548924. JRR, AA, DG, JZP acknowledge support from the NSF Award #16484510.

Disclosures

The authors declare no conflicts of interest.

Data Availability

Data are not publicly available at this time but may be obtained from the authors upon reasonable request.

Code Availability

The GUI for mask selection, the code used to train the model and the trained model (Python and MATLAB implementations) are available at: <https://github.com/chaetries/mmTissueFilter>.

References

- [1] Nirmalya Ghosh and I Alex Vitkin. Tissue polarimetry: concepts, challenges, applications, and outlook. *Journal of Biomedical Optics*, 16(11):110801–110801, 2011.
- [2] C. He, H. He, J. Chang, B. Chen, H. Ma, and M. J. Booth. Polarisation optics for biomedical and clinical applications: a review. *Light Sci. Appl.*, 22(10):194, 2021.
- [3] Ji Qi and Daniel S Elson. Mueller polarimetric imaging for surgical and diagnostic applications: a review. *Journal of Biophotonics*, 10(8):950–982, 2017.
- [4] Jessica C Ramella-Roman and Tatiana Novikova. *Polarized Light in Biomedical Imaging and Sensing*. Springer Cham, 2023.
- [5] Shane Rober Cloude. Group theory and polarisation algebra. *Optik (Stuttgart)*, 75(1):26–36, 1986.
- [6] Tatiana Novikova, Alexey Ovchinnikov, Gleb Pogudin, and Jessica C Ramella-Roman. Time-efficient filtering of imaging polarimetric data by checking physical realizability of experimental Mueller matrices. *Bioinformatics*, 40(7):btae348, 06 2024.
- [7] Sooyong Chae, Tongyu Huang, Omar Rodríguez-Núñez, Théotim Lucas, Jean-Charles Vanel, Jérémie Vizet, Angelo Pierangelo, Gennadii Piavchenko, Tsanislava Genova, Ajmal Ajmal, et al. Machine learning approach to 3×4 Mueller polarimetry for complete reconstruction of diagnostic polarimetric images of biological tissues. *IEEE Trans. Med. Imaging*, 44(9):3820–3831, 2025.
- [8] Joseph Chue-Sang, Yuqiang Bai, Susan Stoff, Mariacarla Gonzalez, Nola Holness, Jefferson Gomes, Ranu Jung, Amir Gandjbakhche, Viktor V Chernomordik, and Jessica C Ramella-Roman. Use of Mueller matrix polarimetry and optical coherence tomography in the characterization of cervical collagen anisotropy. *Journal of Biomedical Optics*, 22(8):086010–086010, 2017.

[9] Joseph Chue-Sang, Nola Holness, Mariacarla Gonzalez, Joan Greaves, Ilyas Saytashev, Susan Stoff, Amir Gandjbakhche, Viktor V Chernomordik, Gene Burkett, and Jessica C Ramella-Roman. Use of Mueller matrix colposcopy in the characterization of cervical collagen anisotropy. *Journal of Biomedical Optics*, 23(12):121605–121605, 2018.

[10] Hee Ryung Lee, Ilyas Saytashev, Vinh Nguyen Du Le, Mala Mahendroo, Jessica Ramella-Roman, and Tatiana Novikova. Mueller matrix imaging for collagen scoring in mice model of pregnancy. *Sci. Rep.*, 11(1):15621, 2021.

[11] Jessica C Ramella-Roman, Mala Mahendroo, Clothilde Raoux, Gaël Latour, and Marie-Claire Schanne-Klein. Quantitative assessment of collagen remodeling during a murine pregnancy. *ACS Photonics*, 11(9):3536–3544, 2024.

[12] Shih-Yau Lu and Russell A. Chipman. Interpretation of Mueller matrices based on polar decomposition. *J. Opt. Soc. Am. A*, 13(5):1106–1113, May 1996.

[13] Hee Ryung Lee, Thomas Sang Hyuk Yoo, Pengcheng Li, Christian Lotz, Florian K. Groeber-Becker, Sofia Dembski, Enric Garcia-Caurel, Razvigor Ossikovski, and Tatiana Novikova. Mueller microscopy of anisotropic scattering media: theory and experiments. In *Proc. SPIE, Unconventional Optical Imaging*, volume 10677, page 1067718, 2018.

[14] H. R. Lee, C. Lotz, F. Kai Groeber-Becker, S. Dembski, and T. Novikova. Digital histology with Mueller polarimetry and FastDBSCAN. *Appl. Opt.*, 61(32):9616–9624, 2022.

[15] Olaf Ronneberger, Philipp Fischer, and Thomas Brox. U-net: Convolutional networks for biomedical image segmentation. In *Medical Image Computing and Computer-Assisted Intervention. Lecture Notes in Computer Science*, volume 9351, pages 234–241. Springer Cham, 2015.

[16] Kaiming He, Xiangyu Zhang, Shaoqing Ren, and Jian Sun. Deep residual learning for image recognition. In *IEEE Conf. Comput. Vis. Pattern Recognit.*, pages 770–778, 2016.

[17] Riverbank Computing Limited. PyQt5: Python bindings for qt5. <https://www.riverbankcomputing.com/software/pyqt/>, 2021. Access: 2025-01-15.

[18] Jia Deng, Wei Dong, Richard Socher, Li-Jia Li, Kai Li, and Li Fei-Fei. Imagenet: A large-scale hierarchical image database. In *IEEE Conf. Comput. Vis. Pattern Recognit.*, pages 248–255, 2009.

[19] Jonathan Long, Evan Shelhamer, and Trevor Darrell. Fully convolutional networks for semantic segmentation. In *IEEE Conf. Comput. Vis. Pattern Recognit.*, pages 3431–3440, 2015.

[20] Sergey Ioffe and Christian Szegedy. Batch normalization: Accelerating deep network training by reducing internal covariate shift. In *Proc. 32nd International Conference on Machine Learning*, pages 448–456, 2015.

[21] Fausto Milletari, Nassir Navab, and Seyed-Ahmad Ahmadi. V-net: Fully convolutional neural networks for volumetric medical image segmentation. In *IEEE 4th International Conference on 3D Vision (3DV)*, pages 565–571, 2016.

[22] Ilya Loshchilov and Frank Hutter. Decoupled weight decay regularization. *arXiv preprint arXiv:1711.05101*, 2017.

[23] Adam Paszke, Sam Gross, Francisco Massa, Adam Lerer, James Bradbury, Gregory Chanan, Trevor Killeen, Zeming Lin, Natalia Gimelshein, Luca Antiga, et al. Pytorch: An imperative style, high-performance deep learning library. In *Advances in Neural Information Processing Systems 32*, volume 1, page 7994, 2019.

[24] Paulius Micikevicius, Sharan Narang, Jonah Alben, Gregory Diamos, Erich Elsen, David Garcia, Boris Ginsburg, Michael Houston, Oleksii Kuchaiev, Ganesh Venkatesh, et al. Mixed precision training. *arXiv preprint arXiv:1710.03740*, 2017.